

Optical properties of graphene quantum dots: the role of chiral symmetry

Denis M Basko¹, Ivan Duchemin², Xavier Blase³

¹ Université Grenoble Alpes and CNRS, LPMMC, 38042 Grenoble, France

² Université Grenoble Alpes and CEA, IRIG-MEM-L.Sim, 38000 Grenoble, France

³ Université Grenoble Alpes and CNRS, Institut Néel, 38042 Grenoble, France

Abstract. We analyse the electronic and optical properties of graphene quantum dots (GQD) using accurate *ab initio* many-body *GW* and Bethe-Salpeter calculations. We show that most pristine GQD, including structures with irregular shapes, are characterized by dark low energy singlet excitations that quench fluorescence. We rationalize this property by exploiting the chiral symmetry of the low energy electronic states in graphene. Edge sp^3 functionalization is shown to efficiently brighten these low lying excitations by distorting the sp^2 backbone planar symmetry. Such findings reveal an original indirect scenario for the influence of functionalization on the photoluminescence properties.

Submitted to: *2D Mater.*

1. Introduction

The fluorescence properties of graphene quantum dots (GQDs), namely small-size monolayer or multilayer graphene flakes [1, 2, 3, 4, 5, 6, 7, 8, 9, 10, 11, 12], are attracting significant interest for potential applications in optoelectronic [11] including bioimaging [4, 5, 6, 9, 10, 12], photovoltaic [3, 10], sensing [5, 9] or photocatalytic [2, 5, 10] devices. The nature of the emitting states, at the core of these properties, is hindered by the large variety of top-down and bottom-up available synthesis techniques. The possible candidates may range from intrinsic $\pi - \pi^*$ transitions, in a confined sp^2 system, to edge states, including e. g. oxygen-rich functional groups or carbene-like zigzag sites. As a result, the main factors influencing the emission wavelength are still much debated.

Pristine GQD properties have been explored at the density functional theory (DFT) and time-dependent TD-DFT levels clearly emphasizing the opening of the photoemission and optical gaps by quantum confinement with decreasing GQD size [13, 14]. Further work demonstrated that functionalization [15, 8, 14, 16, 17, 18] and/or doping [14, 19, 20, 21, 22] can significantly affect the electronic and optical properties of GQDs. While such studies shed some light on the large variety of photoluminescence properties that can be observed experimentally given the chosen synthesis route and edge treatment, some intriguing properties of pristine GQDs were reported [23, 24, 25, 26, 27, 28]. In particular, the lowest excitations were found to have very small optical transition dipoles. This can manifest itself in a large Stokes shift between absorption and luminescence peaks, or, if efficient non-radiative decay channels are present, in quenching of the photoluminescence. These properties were associated with the high geometrical symmetry of the considered ideal flakes [24, 26, 28].

In the present study, we show that the presence of low lying dark excitations in pristine GQDs is a general property rooted in the hexagonal symmetry of the underlying graphene lattice and the electron-hole chiral symmetry. Moreover, this property is preserved also for structures deviating significantly from high symmetry shapes. These conclusions are confirmed by *ab initio* many-body Green's function calculations performed on realistic GQDs. We argue that the chiral symmetry imposes a certain hierarchy of energy scales which (i) persists even when the spatial symmetries are

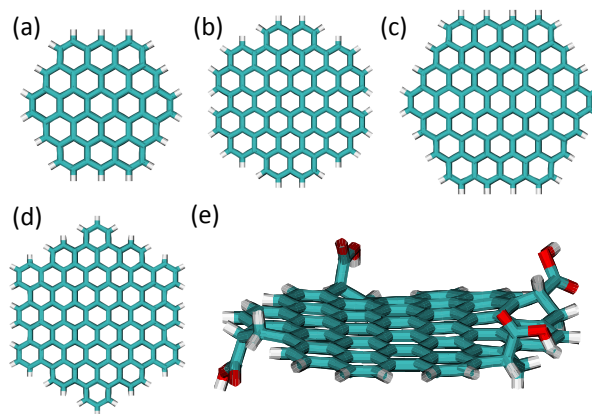


Figure 1. High-symmetry GQDs with (a) 72, (b) 108, (c) 120 and (d) 144 total number of atoms. Structure (e) is the 108-atoms GQD with four -COOH groups functionalizing H-passivated C-atom resulting in a local sp^3 configuration. Relative sizes are not respected.

lifted and (ii) results in the lowest singlet excitation being dark. We show that sp^3 functionalization of the kind observed experimentally very efficiently brightens the low lying dark states by breaking the planarity of the GQDs. As such, edge functional groups strongly impact indeed the GQDs photoluminescence even though not contributing directly to the emission process.

2. Methodology

The electronic and optical properties of pristine and functionalized GQDs are studied using the *ab initio* many-body GW [29] and Bethe-Salpeter equation (BSE) formalisms [30, 31]. The BSE approach was shown in particular to provide a balanced and accurate description of both Frenkel and charge-transfer optical singlet excitations in molecular systems [32]. Our calculations are performed with the FIESTA package [33, 34] at the 6-311Gd eigenvalue-self-consistent $evGW@PBE0$ level, where the corrected electronic energy levels are re-injected self-consistently in the construction of G and W for sake of accuracy [35, 36]. Our calculations are performed using the Coulomb-fitting resolution of the identity (RI-V) [37, 38] together with the auxiliary Weigend Coulomb-fitting basis set [39]. The dynamical self-energy is calculated using the contour-deformation approach [40], namely without any plasmon-pole approximation. Structures

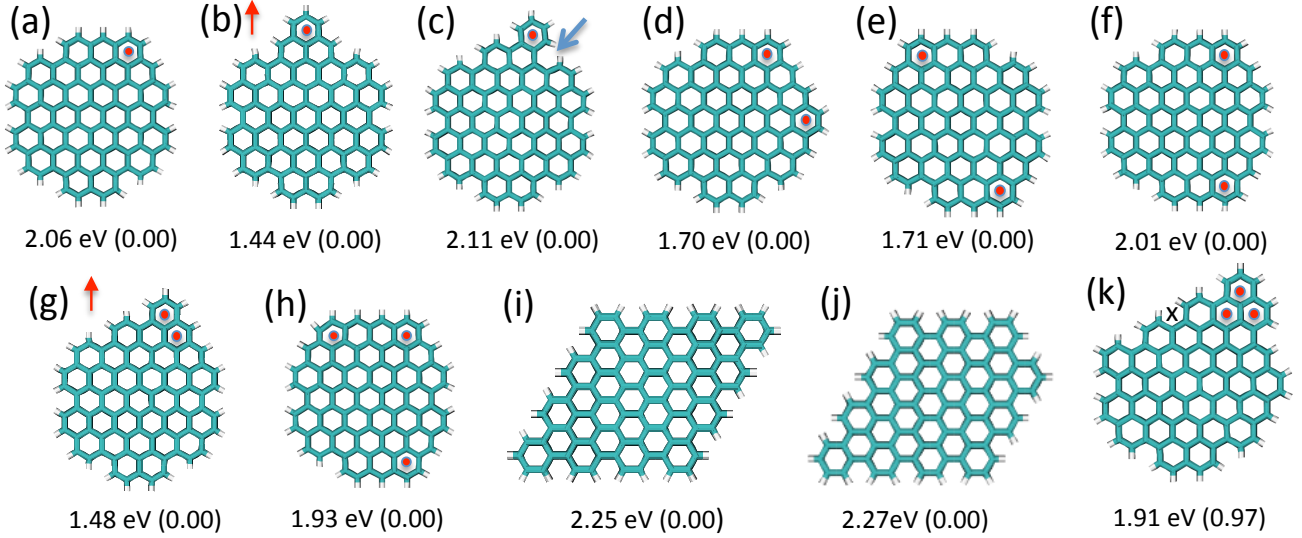


Figure 2. Structures obtained from the 108-atoms GQD of Fig. 1(b) by adding one (a-c), two (d-g) or three (h) rings (red dots), or by removing one ring (cross). Structures (b,g) are open-shell (indicated by red arrows) while in (c) the blue arrow indicates a steric conflict. The associated lowest singlet (S_1) TD-PBE0 excitation energy and oscillator strength (in parenthesis) are indicated below each structure. Information about higher excitations is provided in Appendix A.

N_C	N_{tot}	D	gap	$S_{1/2}^{dark}$	$S^{bright} (f)$
54	72	1.34	4.98	2.20/2.50	3.02 (1.06)
84	108	1.67	4.39	2.01/2.21	2.67 (1.44)
96	120	1.79	3.78	1.60/1.84	2.22 (1.24)
114	144	1.95	4.06	1.92/2.08	2.45 (1.68)

Table 1. Quasiparticle *evGW* HOMO-LUMO energy gaps and BSE lowest optical absorption excitation energies (in eV) for high symmetry GQDs (Fig. 1). Bright states oscillator strengths (f) are indicated. The average diameter D (given in nm) is defined by $N_C A_C = \pi(D/2)^2$, where N_C is the number of carbon atoms, $A_C = 3\sqrt{3}d_{CC}^2/4$ is the area per carbon atom with $d_{CC} = 0.142$ nm. N_{tot} is the total number of atoms (including hydrogen atoms).

are relaxed at the 6-31Gd PBE0 level. BSE calculations are performed beyond the Tamm-Dancoff approximation (TDA).

3. Results

We start by studying high symmetry flakes represented in Fig. 1(a-d) with related data in Table 1. Besides the standard confinement-related increase of the photoemission and optical gaps with decreasing diameter D , we find that the HOMO and the LUMO are always doubly degenerate, consistently with the results of Refs. [24, 27]. We will return to this observation below.

Turning now to the optical properties, a remarkable feature is that the two lowest singlet excitations $S_{1/2}$ are always dark, the first bright excitations being located at higher energy (Table 1). While such prop-

erties were assigned in Ref. [24] to the high symmetry (D_{3h} or D_{6h}) of the two considered GQDs, we now show that the presence of such low-lying dark states is a much more general feature.

We thus explore less symmetric GQDs. Starting from the 108-atoms GQD 1(b), we consider structures obtained by adding one ring in all possible inequivalent positions as depicted in Fig. 2(a-c), together with structures with two added rings [Fig. 2(d-g)], and finally a structure with three added rings [Fig. 2(h)] breaking all symmetries. In addition, an ideal and truncated rhombus-shaped GQD with armchair edges are considered [Fig. 2(i,j)]. To conclude this series, we finally introduced in Fig. 2(k) a structure with a very irregular edge. To facilitate the calculations on such a large number of structures, we first perform TD-DFT calculations at the PBE0/6-311Gd and TDA levels. The lowest singlet excitation (S_1) energy and oscillator strength are provided below each structure. The most salient feature is that the dark nature of the lowest excitation is preserved in most cases even when all symmetries are broken [e. g., structures 2(c,g,h)]. Only the very irregular 2(k) structure presents a bright S_1 , the dark excitation being the S_2 located 0.15 eV above.

For structures shown in Figs. 1(b) and 2(d,h-k), we further perform full *ab initio* BSE calculations which confirm the results obtained at the TD-DFT level. The BSE data are provided in Table 2 for the lowest S_1 singlet excitations with a more complete account in Appendix A (Table A1) for higher lying states, together with a representation of the ordering of

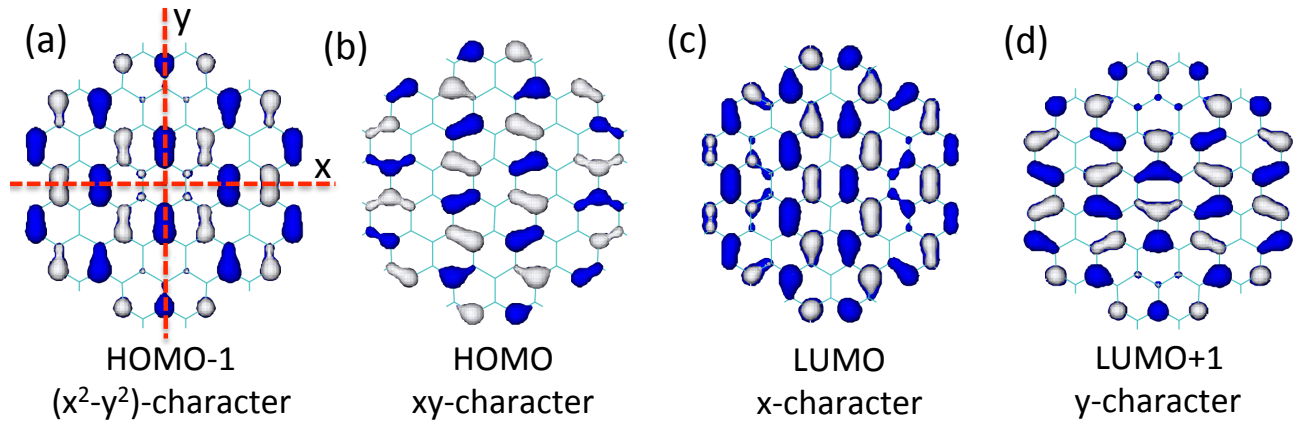


Figure 3. Isocontour representation of the PBE0 Kohn-Sham eigenstates for the frontier orbitals of the highly symmetric 1(b) structure. The dashed red lines indicate in-plane axes as a guide to the eyes.

dark and bright excitations for such systems (Fig. A1). The most salient feature is that again in all cases the lowest singlet excitation is dark, except for the very distorted 2(k) structure for which the lowest bright excitation goes below the dark one with a 0.19 eV energy difference.

We now provide a very general rationale on why most pristine GQDs present a dark lowest energy singlet, except GQDs with very irregular edge such as the 2(k) structure for which the S_1 excitation is suddenly brightened. We start by analyzing the single-electron energy levels and then proceed with the effect of the electron-hole interaction on the excited states, revealing the energy competition that stabilizes/destabilizes bright and dark states.

4. Discussion: single-particle states

To understand the structure of single-electron orbitals, let us first consider a GQD with C_{6v} symmetry (we do not exploit the full D_{6h} symmetry of the structures in Fig. 1). C_{6v} has 4 one-dimensional irreducible representations and 2 two-dimensional ones, E_1 and E_2 represented by the functions $(x, y) \sim E_1$ and $(x^2 - y^2, 2xy) \sim E_2$. The four zero-energy states at the Dirac point of an infinite crystal form a representation of C_{6v} which is reducible as $E_1 + E_2$. In order to have the largest overlap with the graphene zero-energy states, the HOMO and LUMO states in a sufficiently large GQD should also correspond to E_1 and E_2 (or vice versa) and thus be doubly degenerate. The plot of the eigenstates, given in Fig. 3 for the case of the 1(b) structure, clearly confirms this analysis. Moreover, dipole transitions between E_1 and E_2 are allowed.

When the symmetry is lowered, the degeneracy is lifted. Still, in all structures we studied, the splitting between HOMO and HOMO-1 or LUMO and LUMO+1 ($\Delta_{H-1,H}$ and $\Delta_{L,L+1}$, respectively)

remains small enough so that the lowest bright and dark excitations are mostly built from transitions between the HOMO-1, HOMO and LUMO, LUMO+1 levels. This was noted in Refs. [24, 16] for symmetric structures, and is also confirmed by the analysis of our BSE eigenstates (see Table A1 in Appendix A and discussion below).

Besides the overall point group symmetry, another crucial symmetry arises from the nearest-neighbour tight-binding (NNTB) model description that, in spite of its simplicity, captures many properties of graphene [41]. The NNTB Hamiltonian has a chiral symmetry: it has matrix elements only between atoms from different sublattices (A and B) of the honeycomb lattice, but not between atoms on the same sublattice. Then, for each single-electron eigenstate with an energy ε (counted from the Dirac point) and a wave function $\phi(\mathbf{r}) = \phi_A(\mathbf{r}) + \phi_B(\mathbf{r})$, where ϕ_A and ϕ_B have supports near A and B atoms, respectively, the wave function $\phi_A(\mathbf{r}) - \phi_B(\mathbf{r})$ also corresponds to an eigenstate whose energy is $-\varepsilon$. The true microscopic Hamiltonian does not have the exact chiral symmetry due to second-nearest-neighbour coupling and the variation of onsite energies for edge carbon atoms. Still, as demonstrated here below by our many-body *ab initio* calculations, the chiral symmetry signature is still present. As a first illustration, we see from Table 2 that $\Delta_{H-1,H}$ and $\Delta_{L,L+1}$ are very close for all structures.

The resulting picture of the four lowest-energy electronic excitations that we denote by $\{X_1, \dots, X_4\}$ is summarized in Fig. 4. Due to the chiral symmetry, we can write the single-particle wavefunctions of HOMO, LUMO and HOMO - 1, LUMO + 1 as

$$\phi_{H,L} = \phi_A \mp \phi_B, \quad \phi_{H-1,L+1} = \tilde{\phi}_A \mp \tilde{\phi}_B. \quad (1)$$

The chiral symmetry requires that excitations X_2 and X_3 are degenerate even if the GQD shape is not

	$\Delta_{H-1,H}$	$\Delta_{H,L}$	$\Delta_{L,L+1}$	d_{2x}, d_{2y}	d_{3x}, d_{3y}	S_1 energy	f	$\{X_i\}$ -weights
1(b)	0.000	4.181	0.000	4.48, 0.01	4.48, 0.01	2.01	0.000	
2(d)	0.137	4.020	0.143	2.31, -4.11	2.30, -4.09	1.86	0.000	0.48 X_2 + 0.48 X_3
2(h)	0.222	3.856	0.228	4.35, -2.00	4.39, -2.03	1.81	0.000	0.48 X_2 + 0.48 X_3
2(j)	0.276	4.295	0.288	3.54, 2.05	3.45, 2.00	2.21	0.000	0.47 X_2 + 0.45 X_3
2(i)	0.351	4.151	0.363	3.62, 2.10	3.67, 2.13	2.18	0.000	0.47 X_2 + 0.46 X_3
2(k)	0.632	3.590	0.633	-2.77, 3.27	-2.70, 3.24	1.79	0.711	0.97 X_1 + 0.02 X_4

Table 2. *Ab initio* GW single-particle level spacings (in eV) for selected structures from Figs. 1 and 2, ordered according to the splitting $\Delta_{H-1,H}$, together with the dipole matrix elements $\mathbf{d}_2, \mathbf{d}_3$ (in atomic units). The two last columns give information on the lowest Bethe-Salpeter S_1 singlet eigenstates, namely energy (in eV), oscillator strength f , and dominant coefficients (squared) on the $\{X_i\}$ transitions (see Fig. 4). In the case of the 1(b) structure, the HOMO and LUMO 2-fold degeneracy hinders such a decomposition.

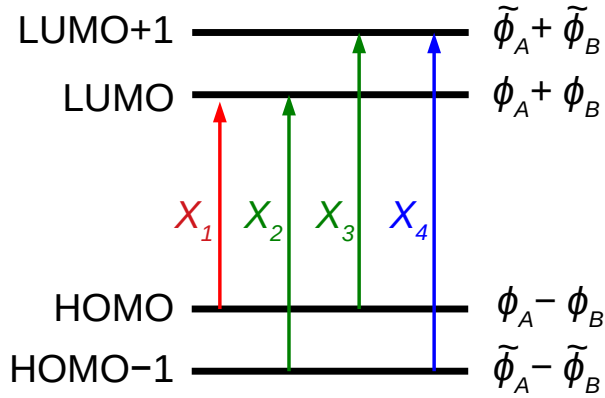


Figure 4. Electronic excitations built from the two highest occupied (HOMO - 1 and HOMO) electronic energy levels and symmetric lowest unoccupied (LUMO and LUMO + 1) energy levels with associated wavefunctions.

symmetric. Moreover, the dipole matrix elements associated with transitions X_2, X_3 given by:

$$\mathbf{d}_2 = \langle \tilde{\phi}_A - \tilde{\phi}_B | \mathbf{r} | \phi_A + \phi_B \rangle, \quad (2)$$

$$\mathbf{d}_3 = \langle \phi_A - \phi_B | \mathbf{r} | \tilde{\phi}_A + \tilde{\phi}_B \rangle, \quad (3)$$

are both equal to $\langle \phi_A | \mathbf{r} | \tilde{\phi}_A \rangle - \langle \phi_B | \mathbf{r} | \tilde{\phi}_B \rangle$ since wavefunctions on sublattices A and B do not overlap. Again, in our microscopic BSE calculations not assuming the chiral symmetry, the resulting dipoles are very close (within 3%; see Table 2). As a result, the linear combination $(X_2 - X_3)/\sqrt{2}$ is *dark*. We now rationalize why this combination often becomes the lowest-energy excitation.

5. Discussion: electron-hole interactions

The dominant resonant part of the 2-body electron-hole BSE Hamiltonian in the $\{X_1, \dots, X_4\}$ basis reads:

$$H_{ia,jb}^{BSE} = (\varepsilon_a - \varepsilon_i) \delta_{ij} \delta_{ab} + 2V_{ia,bj}^x - W_{ij,ab}^d, \quad (4)$$

where $(i, j)/(a, b)$ label occupied/empty single-particle levels, respectively, and:

$$V_{ia,bj}^x = \int \phi_i(\mathbf{r}) \phi_a(\mathbf{r}) V(\mathbf{r} - \mathbf{r}') \phi_b(\mathbf{r}') \phi_j(\mathbf{r}') d\mathbf{r} d\mathbf{r}',$$

$$W_{ij,ab}^d = \int \phi_i(\mathbf{r}) \phi_j(\mathbf{r}) W(\mathbf{r}, \mathbf{r}') \phi_a(\mathbf{r}') \phi_b(\mathbf{r}') d\mathbf{r} d\mathbf{r}',$$

are matrix elements of the bare and screened Coulomb potential, respectively. Selected *ab initio* matrix elements for the considered structures are given in Table 3. Their inspection reveals several common properties.

(i) The diagonal elements $W_{\alpha\alpha}^d$ are by far dominant and have close values. This is a consequence of the long-range nature of the Coulomb interaction and orthogonality of the single-electron wave functions: if one takes the limit of the infinite-range interaction for V and W , namely $V(\mathbf{r} - \mathbf{r}') = W(\mathbf{r}, \mathbf{r}') \rightarrow \text{const}$, the integrals over \mathbf{r} and \mathbf{r}' separate and vanish by orthogonality everywhere except $W_{\alpha\alpha}^d$ which are all equal.

(ii) Both $V_{\alpha\beta}^x$ and $W_{\alpha\beta}^d$ are small if $\alpha \in \{1, 4\}$ and $\beta \in \{2, 3\}$. In fact, they must vanish for structures 1(b), 2(d,i,j) because of the remaining mirror symmetry [42]. Indeed, HOMO and HOMO - 1 must have different parity with respect to this mirror reflection, and the same holds for LUMO and LUMO + 1; this follows from the reduction of the two-dimensional E_1 and E_2 representations of the C_{6v} group to a simple mirror one. Since the Coulomb potential is even, the corresponding integrals must vanish. For QDs which do not have exact mirror symmetry, these integrals remain small.

(iii) The diagonal $V_{\alpha\alpha}^x > 0$, because the Coulomb potential $V(\mathbf{r} - \mathbf{r}')$ is positive in the operator sense.

(iv) $V_{22}^x \approx V_{33}^x \approx V_{23}^x$. In fact, if one uses the representation (1) of the single-particle wave functions and neglects the overlap between A and B components, all three integrals become $\langle \phi_A \tilde{\phi}_A - \phi_B \tilde{\phi}_B | V | \phi_A \tilde{\phi}_A - \phi_B \tilde{\phi}_B \rangle$, another signature of the underlying chiral symmetry.

(v) $W_{23}^d \ll V_{23}^x$. In the representation of Eq. (1), these matrix elements have the form $\langle \phi_A \tilde{\phi}_A \pm \phi_B \tilde{\phi}_B | V | \phi_A \tilde{\phi}_A \pm \phi_B \tilde{\phi}_B \rangle$ with the $+/-$ sign corresponding to W_{23}^d/V_{23}^x , respectively. V_{23}^x is mostly the dipole-dipole interaction between \mathbf{d}_2 and \mathbf{d}_3 . In

	V_{11}^x	V_{22}^x	V_{33}^x	V_{12}^x	V_{23}^x	W_{11}^d	W_{22}^d	W_{33}^d	W_{12}^d	W_{23}^d
1(b)	0.400	0.333	0.331	10^{-4}	0.313	2.349	2.313	2.313	10^{-4}	0.018
2(d)	0.500	0.346	0.345	10^{-4}	0.329	2.341	2.257	2.261	10^{-4}	0.036
2(h)	0.494	0.341	0.341	0.008	0.325	2.280	2.231	2.235	-0.007	0.032
2(j)	0.435	0.232	0.234	10^{-5}	0.216	2.331	2.273	2.276	10^{-5}	0.018
2(i)	0.448	0.220	0.225	10^{-4}	0.206	2.271	2.226	2.242	10^{-5}	0.011
2(k)	0.471	0.317	0.317	-0.033	0.304	2.283	2.201	2.207	-0.018	0.077

Table 3. *Ab initio* Bethe-Salpeter matrix elements (in eV) for selected structures from Figs. 1 and 2, ordered according to the splitting $\Delta_{H-1,H}$.

contrast, for the symmetric 1(b) and 2(i) structures, the dipole moment of the $\phi_H\phi_{H-1}$ and $\phi_L\phi_{L+1}$ co-densities vanishes by symmetry, so that W_{23}^d stems from a weaker quadrupole-quadrupole interaction. For other structures with reduced symmetry, the codensity dipoles remain significantly smaller than $\mathbf{d}_{2/3}$.

Moreover, for the $\phi_H\phi_{H-1} = \phi_L\phi_{L+1} = \phi_A\tilde{\phi}_A + \phi_B\tilde{\phi}_B$ co-densities we find a strong sign alternation on adjacent A/B sites, which persists even in the absence of spatial (point group) symmetries. This leads to a further suppression of W_{23}^d due to the smooth long-range nature of the Coulomb potential, so that for rapidly oscillating functions the integral is small. We rationalize this observation in Appendix B.

These properties determine the energy ordering of the optical excitations. The large diagonal matrix elements $W_{\alpha\alpha}^d$ provide an overall shift without affecting much the ordering, by virtue of property (i). Due to property (ii), the $\{X_2, X_3\}$ and $\{X_1, X_4\}$ blocks do not couple and can be analyzed separately. This is confirmed by the stable and dominant weights of the BSE lowest dark states on the $X_{2/3}$ transitions (see Table 2) irrespective of the $\Delta_{H-1,H}$ splitting. Similarly, the lowest BSE bright states are built dominantly from X_1 and X_4 contributions (see structure 2(k) in Table 2 and Table A1 in Appendix A). In the $\{X_2, X_3\}$ block, the degeneracy is lifted essentially by V_{23}^x [property (v)] which pushes up in energy the bright combination $(X_2 + X_3)/\sqrt{2}$ by $4V_{23}^x$ and leaves the energy of the dark combination unaffected, due to properties (iii,iv). In the $\{X_1, X_4\}$ sector, the main effect is to push up X_1 by $2V_{11}^x$ [property (iii)]; the mixture with X_4 and the corresponding level repulsion is less important since X_1 and X_4 were split in the very beginning because of the single-particle energy difference between Δ_{HL} and $\Delta_{H-1,L+1}$ when the degeneracies of HOMO and LUMO are broken. In particular, for structure 2(k) with largest $\Delta_{H-1,H}$ splitting, the lowest bright excitation is dominated by the X_1 HOMO-LUMO transition (see Table 2). In practice, $(X_2 + X_3)/\sqrt{2}$ and X_4 are high enough in energy, so that they mix with higher excitations.

Overall, the difference in energy between the dark $(X_2 - X_3)/\sqrt{2}$ and bright X_1 excitations read:

$$E^{\text{dark}} - E^{\text{bright}} = \Delta_{H-1,H} + W_{23}^d + W_{11}^d - W_{22}^d - 2V_{11}^x$$

with $W_{23}^d \simeq 0$ and $(W_{11}^d - W_{22}^d) \simeq 0$. As a result, the relative position of the lowest X_1 -like bright excitation and the $(X_2 - X_3)$ dark combination depends on the competition between the energy splitting $\Delta_{H-1,H} \approx \Delta_{L-1,L}$ pushing the dark state up, and the diagonal exchange integral $2V_{11}^x$ that pushes X_1 up. Thus, for high-symmetry GQDs with degenerate HOMOs and LUMOs, the lowest excitation is always dark. Upon breaking the point-group symmetry, the level splitting $\Delta_{H-1,H} \approx \Delta_{L-1,L}$ increases as the shape of the dot becomes more irregular. Still, the lowest excitation remains the dark one as long as the splitting remains small compared to the energy scale which can be roughly estimated as $2V_{11}^x$.

The non-zero contributions from the W_{23}^d and $(W_{11}^d - W_{22}^d)$ terms, due to deviations of the BSE *ab initio* Hamiltonian from the NNTB model, the small coupling of the X_1 state with the higher-lying X_4 contribution, and the non-resonant contributions in our full (beyond TDA) BSE calculations, explain that the criterion on the sign of $(\Delta_{H-1,H} - 2V_{11}^x)$ is not strictly quantitative. This is the reason why the structure 2(k) has a bright ground state while the splitting is still smaller than $2V_{11}^x$.

These findings are reminiscent of carbon nanotubes with the presence of low-lying dark excitations related to the mixing and stabilization by Coulomb interaction of degenerate single-particle transitions [43]. Due to reduced confinement and enhanced screening as compared to GQDs, differences of energy between bright and dark excitonic states in nanotubes were found to be of the order of a few meV [44], namely, much smaller than what we observe here. Similar effects have been revealed in the case of nanoribbons but with a strong dependence on the edge structure (the “geometric chirality”, which must not be confused with the chiral symmetry we consider in the present paper) that governs the presence of degenerate single-particle transitions at low energy [45]. We emphasize however that what we addressed here is the case of finite size

systems with irregular edges, revealing the properties leading to the “protection” of the low-lying dark states upon breaking of the ideal geometry and lifting of the single-particle transition degeneracies.

6. Effect of functionalization

To confirm the importance of the chiral symmetry, we finally consider the experimental observation that most photoluminescent GQDs are functionalized with nitrogen or oxygen-rich side groups [1, 2, 3, 4, 5, 6, 11, 12]. Taking as a paradigmatic example the 108-atoms GQD (Fig. 1b), we first replace four passivating H atoms by carboxyl -COOH groups, leaving all carbon atoms in an sp^2 configuration. Such a functionalization hardly lifts the HOMO and LUMO degeneracy and leaves the 2 lowest excitation dark. On the contrary, adding the carboxyl groups to already H-functionalized C atoms, namely, creating sp^3 edge carbon atoms [see Fig. 1(e)], significantly increases the S_1 oscillator strength from zero to 0.25. Our conclusion is that the asymmetric functionalization (one H atom, one carboxyl group) significantly distorts the flake that starts deviating from its ideal sp^2 planar geometry, breaking the underlying conditions for chiral symmetry. Replacing the COOH group by an H atom that we fully relax but keeping all C atoms frozen to their distorted geometry, we find that the S_1 excitation remains bright with an energy and oscillator strength that hardly changes.

Exploring all possible ways to distort planar GQDs by functionalization (see e.g. Ref. [15]) is beyond the scope of the present study. We can conclude however that sp^3 functionalization provides an important pathway to increase emission from GQDs by brightening the lowest singlet excitations populated by Kasha’s rule after relaxation of hot electrons. We emphasize however that such a behaviour does not directly involve the electronic properties of the side groups that just serve as a mean to induce a structural distortion breaking the chiral symmetry. The sp^3 character of edge atoms was revealed explicitly in a few studies by XPS measurements [7, 12]. Such a picture allows to make a possible connection between GQDs and graphene oxide that can be described as sp^2 islands in an sp^3 matrix [13, 46].

7. Structural relaxation in the excited state

To conclude this exploration, we now study the effect of relaxation in the excited state. We turn again to TD-DFT calculations at the PBE0/6-311Gd level within the Tamm-Dancoff approximation for sake of numerical efficiency. The lack of analytic forces in the BSE formalism precludes relaxations in the excited state.

The good agreement between TD-PBE0 and BSE data concerning the energy and nature (bright or dark) of the lowest absorption singlet states, allows to conclude that both TD-DFT and BSE convey the same physical picture. This is an indirect signature that the systems we study are not presenting charge-transfer states that would result in difficulties for TD-PBE0.

Upon relaxation in the S_1 state, the GQD-72 (Fig. 1a) lowest excitation energy is redshifted from 2.33 eV to 2.26 eV (TD-DFT values), but the lowest S_1 state remains completely dark. Similarly, the GQD-108 (Fig. 1b) singlet absorption onset S_1 is redshifted upon relaxation from 2.24 eV to 2.07 eV remaining completely dark. Clearly, relaxation in the excited state induces a marginal effect on the emission energy for such pristine GQDs. Turning now to the structure with sp^2 -preserving functionalization, we find again that relaxation shifts the S_1 energy by about 0.06 eV, from 2.07 eV to 2.01 eV, but without changing its dark state nature.

Finally, relaxation of the sp^3 -functionalized (Fig. 1e) system results in a 0.1 eV redshift of the lowest excited state (from 2.12 to 2.02 eV), its oscillator strength changing from 0.31 to 0.43 (TD-PBE0/TDA values). These selected results clearly indicate that relaxation in the S_1 excited state does not affect the conclusions drawn here above in the study of the lowest absorption features.

8. Conclusions

In conclusion, we demonstrated that pristine GQDs present in general a dark lowest singlet excitation as a result of the underlying chiral symmetry, irrespective of the overall geometrical point-group symmetry. The relation between electron and hole wavefunctions on sublattices A and B, as induced by the local chiral symmetry in graphene, ensures that there is always a dark combination of the (HOMO) \rightarrow (LUMO+1) and (HOMO-1) \rightarrow LUMO transitions that lies in general lower in energy than the bright HOMO \rightarrow LUMO excitation destabilized by exchange Coulomb interaction. Only very distorted structures, characterized by a large HOMO-(HOMO-1) or equivalent LUMO-(LUMO+1) splitting destabilizing the dark combination, can bring the bright HOMO-LUMO excitation lower in energy.

While extensive stability calculations may provide insights on the likeliness of very irregular edge structures given the synthesis conditions [47], we conclude that a very large fraction of pristine GQDs, including GQDs without any overall point-group symmetry, present a lowest dark singlet quenching photoluminescence. Such a conclusion is not affected by the weak structural relaxation in the excited state.

Our results indicate that sp^3 edge functionalization is extremely efficient in switching the photoluminescent properties of GQDs. We observe however that it is the breaking of the underlying chiral symmetry, and not necessarily the occurrence of charge-transfer core-to-edge optical excitations, that plays a significant role.

Our results do not exclude other pathways to enhancing photoluminescence. Consistently with early reports on the effect of doping in nanotubes [48], the doping of GQDs [14, 19, 20, 21, 22] also stands as an efficient way to enhance photoluminescence. Following the well known case of graphene [49], the interaction with a substrate may also affect electronic properties close to the gap, with an effect on the photoluminescence related to the interaction strength. Clearly, doping or charge-transfer from a substrate, introduction of in-gap defect-induced levels or associated structural distortions, can break the pristine GQDs electron-hole symmetry. Finally, functional groups optically active in the GQD optical gap can also stand as a way to bypass the presence of these low-lying dark states.

The experimental characterization of such dark states would require the synthesis of undoped GQDs with controlled planar shape and the verification that such systems are poorly photoluminescent. We do not exclude that this has been observed but for obvious reasons emphasis was put on systems with good photoluminescent properties. As a suggestion, comparing functional groups known to favour sp^2 versus sp^3 edge functionalization should allow to relate the photoluminescent properties to the GQD planarity, as sp^3 functionalization is likely to distort significantly the GQD.

Acknowledgments

The authors acknowledge support from the French GENCI supercomputing facilities under contract A0030910016.

References

- [1] Pan D, Zhang J, Li Z and Wu M 2010 *Adv. Mater.* **22** 734–738
- [2] Li H, He X, Kang Z, Huang H, Liu Y, Liu J, Lian S, Tsang C, Yang X and Lee S T 2010 *Angew. Chem. Int. Ed.* **49** 4430–4434
- [3] Li Y, Hu Y, Zhao Y, Shi G, Deng L, Hou Y and Qu L 2011 *Adv. Mater.* **23** 776–780
- [4] Zhu S, Zhang J, Qiao C, Tang S, Li Y, Yuan W, Li B, Tian L, Liu F, Hu R, Gao H, Wei H, Zhang H, Sun H and Yang B 2011 *Chem. Commun.* **47**(24) 6858–6860
- [5] Shen J, Zhu Y, Yang X and Li C 2012 *Chem. Commun.* **48**(31) 3686–3699
- [6] Peng J, Gao W, Gupta B K, Liu Z, Romero-Aburto R, Ge L, Song L, Alemayehu L B, Zhan X, Gao G, Vithayathil S A, Kaiparettu B A, Marti A A, Hayashi T, Zhu J J and Ajayan P M 2012 *Nano Lett.* **12** 844–849
- [7] Tang L, Ji R, Cao X, Lin J, Jiang H, Li X, Teng K S, Luk C M, Zeng S, Hao J and Lau S P 2012 *ACS Nano* **6** 5102–5110
- [8] Jin S H, Kim D H, Jun G H, Hong S H and Jeon S 2013 *ACS Nano* **7** 1239–1245
- [9] Li L, Wu G, Yang G, Peng J, Zhao J and Zhu J J 2013 *Nanoscale* **5**(10) 4015–4039 URL <http://dx.doi.org/10.1039/C3NR33849E>
- [10] Wang L, Wang Y, Xu T, Liao H, Yao C, Liu Y, Li Z, Chen Z, Pan D, Sun L and Wu M 2014 *Nature Comm.* **5** 5357
- [11] Lim S Y, Shen W and Gao Z 2015 *Chem. Soc. Rev.* **44**(1) 362–381
- [12] Ding H, Yu S B, Wei J S and Xiong H M 2016 *ACS Nano* **10** 484–491
- [13] Eda G, Lin Y Y, Mattevi C, Yamaguchi H, Chen H A, Chen I S, Chen C W and Chhowalla M 2010 *Adv. Mater.* **22** 505–509
- [14] Sk M A, Ananthanarayanan A, Huang L, Lim K H and Chen P 2014 *J. Mater. Chem. C* **2**(34) 6954–6960 URL <http://dx.doi.org/10.1039/C4TC01191K>
- [15] Cocchi C, Prezzi D, Ruini A, Caldas M J and Molinari E 2012 *J. Phys. Chem. C* **116** 17328–17335 (*Preprint* <https://doi.org/10.1021/jp300657k>) URL <https://doi.org/10.1021/jp300657k>
- [16] Geethalakshmi K R, Ng T Y and Crespo-Otero R 2016 *J. Mater. Chem. C* **4**(36) 8429–8438 URL <http://dx.doi.org/10.1039/C6TC02785G>
- [17] Chen S, Ullah N, Wang T and Zhang R 2018 *J. Mater. Chem. C* **6**(25) 6875–6883 URL <http://dx.doi.org/10.1039/C8TC02083C>
- [18] Jingang Wang J, Cao S, Ding Y D, Ma Fengcai and Lu W and Sun M 2018 *Sci. Report* **6** 24850
- [19] Niu X, Li Y, Shu H and Wang J 2016 *Nanoscale* **8**(46) 19376–19382 URL <http://dx.doi.org/10.1039/C6NR06447G>
- [20] Noor-Ul-Ain, Eriksson M O, Schmidt S, Asghar M, Lin P C, Holtz P O, Syväjärvi M and Yazdi G R 2016 *Nanomaterials* **6** ISSN 2079-4991
- [21] Feng J, Dong H, Pang B, Shao F, Zhang C, Yu L and Dong L 2018 *Phys. Chem. Chem. Phys.* **20**(22) 15244–15252 URL <http://dx.doi.org/10.1039/C8CP01403E>
- [22] Kadian S, Manik G, Kalkal A, Singh M and Chauhan R P 2019 *Nanotechnology* **30** 435704 URL <https://doi.org/10.1088%2F1361-6528%2F30435704>
- [23] Heiskanen H P, Manninen M and Akola J 2008 *New J. Phys.* **10** 103015 URL <https://doi.org/10.1088%2F1367-2630%2F10%2F10%2F103015>
- [24] Schumacher S 2011 *Phys. Rev. B* **83**(8) 081417 URL <https://link.aps.org/doi/10.1103/PhysRevB.83.081417>
- [25] Zhao M, Yang F, Xue Y, Xiao D and Guo Y 2014 *ChemPhysChem* **15** 950–957 (*Preprint* <https://onlinelibrary.wiley.com/doi/pdf/10.1002/cphc.201301137>) URL <https://onlinelibrary.wiley.com/doi/abs/10.1002/cphc.201301137>
- [26] Ozfidan I, Korkusinski M, Güçlü A D, McGuire J A and Hawrylak P 2014 *Phys. Rev. B* **89**(8) 085310 URL <https://link.aps.org/doi/10.1103/PhysRevB.89.085310>
- [27] Li Y, Shu H, Wang S and Wang J 2015 *J. Phys. Chem. C* **119** 4983–4989
- [28] Pohle R, Kavousanaki E G, Dani K M and Shannon N 2018 *Phys. Rev. B* **97**(11) 115404 URL <https://link.aps.org/doi/10.1103/PhysRevB.97.115404>
- [29] Hedin L 1965 *Phys. Rev.* **139**(3A) A796–A823 URL <https://link.aps.org/doi/10.1103/PhysRev.139.A796>
- [30] Salpeter E E and Bethe H A 1951 *Phys. Rev.* **84**(6) 1232–1242 URL <https://link.aps.org/doi/10.1103/PhysRev.84.1232>
- [31] Hanke W and Sham L J 1979 *Phys. Rev. Lett.* **43**(5) 387–390 URL <https://link.aps.org/doi/10.1103/PhysRevLett.43.387>

- 1103/PhysRevLett.43.387
- [32] Blase X, Duchemin I and Jacquemin D 2018 *Chem. Soc. Rev.* **47**(3) 1022–1043 URL <http://dx.doi.org/10.1039/C7CS00049A>
- [33] Jacquemin D, Duchemin I and Blase X 2015 *J. Chem. Theory Comput.* **11** 3290–3304
- [34] Duchemin I, Guido C A, Jacquemin D and Blase X 2018 *Chem. Sci.* **9**(19) 4430–4443 URL <http://dx.doi.org/10.1039/C8SC000529J>
- [35] Kaplan F, Harding M E, Seiler C, Weigend F, Evers F and van Setten M J 2016 *J. Chem. Theory Comput.* **12** 2528–2541
- [36] Rangel T, Hamed S M, Bruneval F and Neaton J B 2016 *J. Chem. Theory Comput.* **12** 2834–2842
- [37] Ren X, Rinke P, Blum V, Wieferink J, Tkatchenko A, Sanfilippo A, Reuter K and Scheffler M 2012 *New J. Phys.* **14** 053020 URL <https://doi.org/10.1088/2F1367-2630/2F14%2F5%2F053020>
- [38] Duchemin I, Li J and Blase X 2017 *J. Chem. Theory Comput.* **13** 1199–1208 pMID: 28094983 (Preprint <https://doi.org/10.1021/acs.jctc.6b01215>) URL <https://doi.org/10.1021/acs.jctc.6b01215>
- [39] Weigend F 2006 *Phys. Chem. Chem. Phys.* **8**(9) 1057–1065 URL <http://dx.doi.org/10.1039/B515623H>
- [40] Blase X, Attaccalite C and Olevano V 2011 *Phys. Rev. B* **83**(11) 115103 URL <https://link.aps.org/doi/10.1103/PhysRevB.83.115103>
- [41] Castro Neto A H, Guinea F, Peres N M R, Novoselov K S and Geim A K 2009 *Rev. Mod. Phys.* **81**(1) 109–162
- [42] The values 10^{-4} – 10^{-5} correspond to the fact that we did not impose a strict constraint on symmetries during the structural relaxation.
- [43] Zhao H and Mazumdar S 2004 *Phys. Rev. Lett.* **93**(15) 157402 URL <https://link.aps.org/doi/10.1103/PhysRevLett.93.157402>
- [44] Mortimer I B and Nicholas R J 2007 *Phys. Rev. Lett.* **98**(2) 027404 URL <https://link.aps.org/doi/10.1103/PhysRevLett.98.027404>
- [45] Prezzi D, Varsano D, Ruini A, Marini A and Molinari E 2008 *Phys. Rev. B* **77**(4) 041404 URL <https://link.aps.org/doi/10.1103/PhysRevB.77.041404>
- [46] Loh K P, Bao Q, Eda G and Chhowalla M 2010 *Nature Chem.* **2** 1015–1024
- [47] Wassmann T, Seitsonen A P, Saitta A M, Lazzeri M and Mauri F 2008 *Phys. Rev. Lett.* **101**(9) 096402 URL <https://link.aps.org/doi/10.1103/PhysRevLett.101.096402>
- [48] Harutyunyan H, Gokus T, Green A A, Hersam M C, Allegrini M and Hartschuh A 2009 *Nano Lett.* **9** 2010–2014 pMID: 19331347 (Preprint <https://doi.org/10.1021/nl9002798>) URL <https://doi.org/10.1021/nl9002798>
- [49] Zhou S Y, Gweon G H, Fedorov A V, First P N, de Heer W A, Lee D H, Guinea F, Castro Neto A H and Lanzara A 2007 *Nature Materials* **6** 770–775 ISSN 1476-4660 URL <https://doi.org/10.1038/nmat2003>

Appendix A. Analysis of the Bethe-Salpeter excitations

A more detailed account of the BSE excitations characteristics is provided in Table A1. Besides the excitation energy, the associated oscillator strength (in parenthesis) and leading weights of the 2-body eigenstates on the low-energy $\{X_1, \dots, X_4\}$ transitions, but also on higher X_i transitions for excitations above the lowest dark and bright combinations, are provided. The Bethe-Salpeter eigenstates read:

$$\psi_{\lambda}^{BSE}(\mathbf{r}_e, \mathbf{r}_h) = \sum_{ia} A_{\lambda}(ia) \phi_i(\mathbf{r}_h) \phi_a(\mathbf{r}_e) + \sum_{ia} B_{\lambda}(ia) \phi_i(\mathbf{r}_e) \phi_a(\mathbf{r}_h), \quad (\text{A.1})$$

where (i, a) label occupied/empty energy levels and λ the Bethe-Salpeter excitations with increasing energy. Table A1 provides the leading $|A_{\lambda}(ia)|^2$ coefficients. The $B_{\lambda}(ia)$ coefficients represent de-excitations when going beyond the Tamm-Dancoff approximation and are much smaller in magnitude. We use the notations of Fig. 4: X_1 represents the HOMO to LUMO transition, X_2 the HOMO–1 to LUMO transition, X_3 HOMO to LUMO+1, and X_4 HOMO–1 to LUMO+1. In addition, we introduce X_5 (HOMO–2 to LUMO), X_6 (HOMO to LUMO+2) and X_7 (HOMO to LUMO+3). All dark and bright states compiled in Table A1 are represented in Fig. A1.

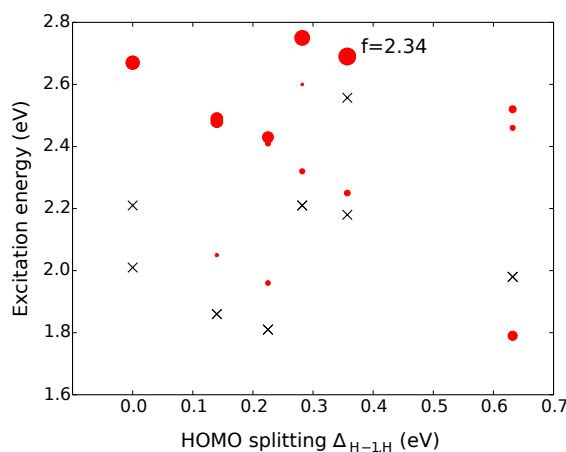


Figure A1. Representation of the data of Table A1 : lowest singlet excitation energies for structures 1(b) and 2(d,h,i-k). The systems are ordered according to the $\Delta_{H-1,H}$ HOMO splitting. Black crosses represent dark states; bright excitations are represented by red circles with a radius proportional to the oscillator strength. The largest (f) oscillator strength is given to set the circle size scale.

	S_1	S_2	S_3	S_4
1(b)	2.01 (0.000)	2.21 (0.000)	2.67 (1.439)	2.67 (1.438)
2(d)	1.86 (0.000) 0.48 X_2 + 0.48 X_3	2.05 (0.091) 0.72 X_1 + 0.26 X_4	2.48 (1.181) 0.44 X_2 + 0.44 X_3	2.49 (1.175) 0.68 X_4 + 0.25 X_1
2(h)	1.81 (0.000) 0.48 X_2 + 0.48 X_3	1.96 (0.188) 0.81 X_1 + 0.18 X_4	2.41 (0.225) 0.46 X_6 + 0.16 X_7	2.43 (1.015) 0.34 X_2 + 0.35 X_3
2(j)	2.21 (0.000) 0.47 X_2 + 0.45 X_3	2.32 (0.220) 0.83 X_1 + 0.14 X_4	2.60 (0.056) 0.51 X_6 + 0.23 X_5	2.75 (1.877) 0.48 X_2 + 0.49 X_3
2(i)	2.18 (0.000) 0.47 X_2 + 0.46 X_3	2.25 (0.281) 0.86 X_1 + 0.11 X_4	2.557 (0.000) 0.48 X_6 + 0.24 X_5	2.69 (2.344) 0.49 X_2 + 0.50 X_3
2(k)	1.79 (0.711) 0.97 X_1 + 0.02 X_4	1.98 (0.000) 0.45 X_2 + 0.46 X_3	2.46 (0.211) 0.60 X_7 + 0.13 X_3	2.52 (0.411) 0.19 X_2 + 0.16 X_3

Table A1. Details on the low-energy Bethe-Salpeter excitations: energy in eV (oscillator strength) and composition, for structures 1(b) and 2(d,h,i,j,k) as indexed in the main text. The dark excitations resulting from a balanced combination of the (X_2) and (X_3) transitions are highlighted in bold (see the definition of X_i transitions in Fig. 4). The composition cannot be determined unambiguously for the first structure because of the doubly degenerate HOMO and LUMO.

Appendix B. Nearest-neighbor tight-binding results

The nearest-neighbor tight-binding model is less precise quantitatively than the *ab initio* calculations, but it is very useful when one needs a qualitative insight into the properties of the wave functions. Here we give the results for the structure from Fig. 2(i) of the main text, a rhombus with armchair edges, possessing the D_{2h} symmetry. Since edge passivation by hydrogen was not included in the tight-binding calculation, no quantitative comparison to the *ab initio* results can be made.

Diagonalization of the tight-binding Hamiltonian, determined by the nearest-neighbor matrix element $\gamma_0 = 3.3$ eV yields 96 single-particle eigenstates $\psi_0, \psi_1, \dots, \psi_{95}$, which we order according to their energies. The important orbitals HOMO-1, HOMO, LUMO and LUMO+1 (ψ_{46} , ψ_{47} , ψ_{48} and ψ_{49} , respectively) are shown in Fig. B1.

To see the effects of the wave function structure on the Coulomb integrals, for both direct and exchange parts, we use the unscreened Coulomb interaction

$$V_{nm} = \begin{cases} \frac{e^2}{|\mathbf{r}_n - \mathbf{r}_m|}, & n \neq m, \\ U, & n = m, \end{cases} \quad (\text{B.1})$$

where n, m label the sites of the honeycomb lattice. The on-site repulsion $U = 15.75$ eV was obtained by evaluating the Coulomb integral on the microscopic p_z orbital of a carbon atom. With this value, the matrix V_{nm} is positive-definite for any GQD shape (indeed, the minimal value of U required to make the matrix V_{nm} positive-definite for an infinite honeycomb lattice with nearest-neighbor distance 1.42 Å is $U_{\min} = 15.64$ eV). The resulting exchange and direct integrals $V_{\alpha\beta}^x$, $V_{\alpha\beta}^d$ in the basis X_1, X_2, X_3, X_4 are given by

(in eV)

$$V^x = \begin{pmatrix} 0.447 & 0. & 0. & -0.315 \\ 0. & 0.244 & 0.244 & 0. \\ 0. & 0.244 & 0.244 & 0. \\ -0.315 & 0. & 0. & 0.311 \end{pmatrix}, \quad (\text{B.2})$$

$$V^d = \begin{pmatrix} 2.660 & 0. & 0. & 0.023 \\ 0. & 2.575 & 0.023 & 0. \\ 0. & 0.023 & 2.575 & 0. \\ 0.023 & 0. & 0. & 2.670 \end{pmatrix}. \quad (\text{B.3})$$

They have the same properties (i)–(v) as the *ab initio* Coulomb integrals, discussed in Sec. 5.

In Fig. B2 we show the co-densities $\psi_{46}\psi_{47}$ and $\psi_{46}\psi_{48}$, responsible for V_{23}^d and V_{23}^x , respectively. Indeed, since $\psi_{46}\psi_{47} = \psi_{48}\psi_{49}$ and $\psi_{46}\psi_{48} = \psi_{47}\psi_{49}$ exactly, due to the chiral symmetry of the nearest-neighbor tight-binding model, we have

$$V_{23}^d = \langle \psi_{46}\psi_{47} | V | \psi_{46}\psi_{47} \rangle, \quad (\text{B.4})$$

$$V_{23}^x = \langle \psi_{46}\psi_{48} | V | \psi_{46}\psi_{48} \rangle. \quad (\text{B.5})$$

The symmetries $\psi_{46}\psi_{47} \sim xy$ (quadrupole), $\psi_{46}\psi_{48} \sim x$ (dipole) follow straightforwardly from the symmetries of the corresponding wave functions. Another striking difference between the two co-densities is that $\psi_{46}\psi_{47}$ exhibits pronounced sign alternation on neighboring sites, while $\psi_{46}\psi_{48}$ represents a rather smooth spatial dependence.

To be more quantitative about the smoothness, and to understand the origin of the sign alternation in $\psi_{46}\psi_{47}$, we introduce the envelope functions. Namely, separating a real wave function $\phi(\mathbf{r})$ into sublattice components, $\phi(\mathbf{r}) = \phi_A(\mathbf{r}) + \phi_B(\mathbf{r})$, we can represent each component $\phi_{A,B}(\mathbf{r})$ as

$$\phi_{A,B}(\mathbf{r}) = \Psi_{A,B}(\mathbf{r}) e^{i\mathbf{K}\mathbf{r}} + \Psi_{A,B}^*(\mathbf{r}) e^{-i\mathbf{K}\mathbf{r}}, \quad (\text{B.6})$$

where $\Psi_{A,B}(\mathbf{r})$ are the smooth envelopes and $\pm\mathbf{K}$ are the inequivalent corners of the first Brillouin zone.

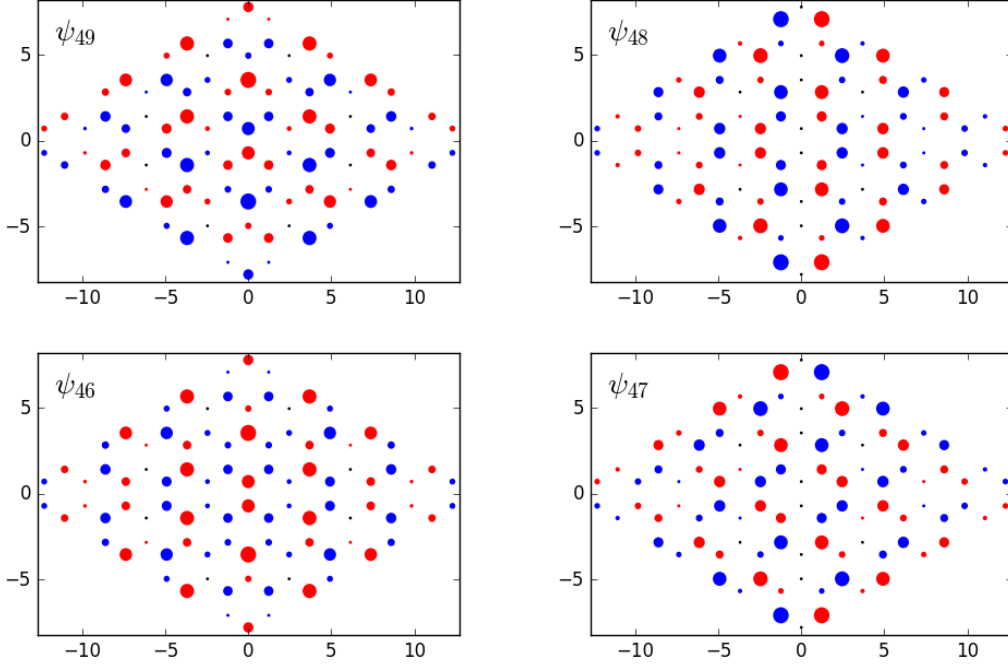


Figure B1. Tight-binding single-particle wave functions ψ_{49} (LUMO+1, energy 1.25 eV, symmetry $\sim y$), ψ_{48} (LUMO, energy 0.96 eV, symmetry $\sim x$), ψ_{47} (HOMO, energy -0.96 eV, symmetry $\sim xy$), ψ_{46} (HOMO-1, energy -1.25 eV, symmetry $\sim x^2 - y^2$) for structure 2(i). The wave functions are real, the color of each circle indicates the sign, while the circle radius represents the absolute value. The carbon atom positions are in angstroms.

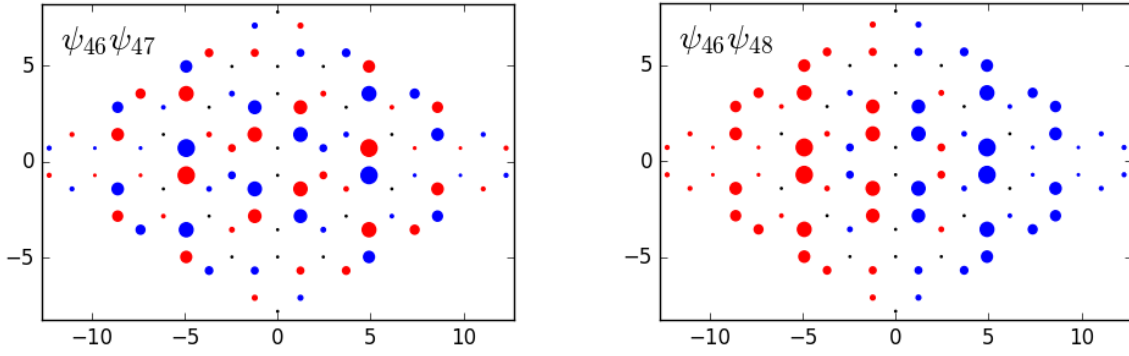


Figure B2. Co-densities $\psi_{46}\psi_{47}$ (left) and $\psi_{46}\psi_{48}$ (right). The color indicates the sign while the dot size represents the absolute value. The positions are in angstroms. Note the sign alternation on neighbouring sites for $\psi_{46}\psi_{47}$.

If the GQD shape is invariant under a reflection $\mathbf{r} \mapsto \mathcal{R}_{AB}\mathbf{r}$ which interchanges the two sublattices but leaves invariant the $\pm\mathbf{K}$ points (for the rhombic shape considered here, it is $y \rightarrow -y$), the wave function $\phi(\mathbf{r})$ is either even or odd, $\phi(\mathbf{r}) = \pm\phi(\mathcal{R}_{AB}\mathbf{r})$. Then, the envelope functions obey $\Psi_{A,B}(\mathcal{R}_{AB}\mathbf{r}) = \pm\Psi_{B,A}(\mathbf{r})$. If the GQD shape is invariant under a reflection $\mathbf{r} \mapsto \mathcal{R}_{\pm\mathbf{K}}\mathbf{r}$ which preserves the two sublattices but flips the $\pm\mathbf{K}$ points (for the rhombic shape considered here, it is $x \rightarrow -x$), the envelope functions obey $\Psi_{A,B}(\mathcal{R}_{\pm\mathbf{K}}\mathbf{r}) =$

$\pm\Psi_{A,B}^*(\mathbf{r})$.

The Fourier transform of each sublattice component for all four orbitals in Fig. B1 is strongly peaked around $\pm\mathbf{K}$. The inverse Fourier transform of the peak around \mathbf{K} determines the smooth envelope functions $\Psi_A(\mathbf{r})$, $\Psi_B(\mathbf{r})$. The complex envelope functions for states 46 and 47 are shown in Figs. B3 and B4 (real and imaginary parts). Due to the chiral symmetry of the nearest-neighbor tight-binding model, $\Psi_{48,A} = \Psi_{47,A}$, $\Psi_{48,B} = -\Psi_{47,B}$, $\Psi_{49,A} = \Psi_{46,A}$,

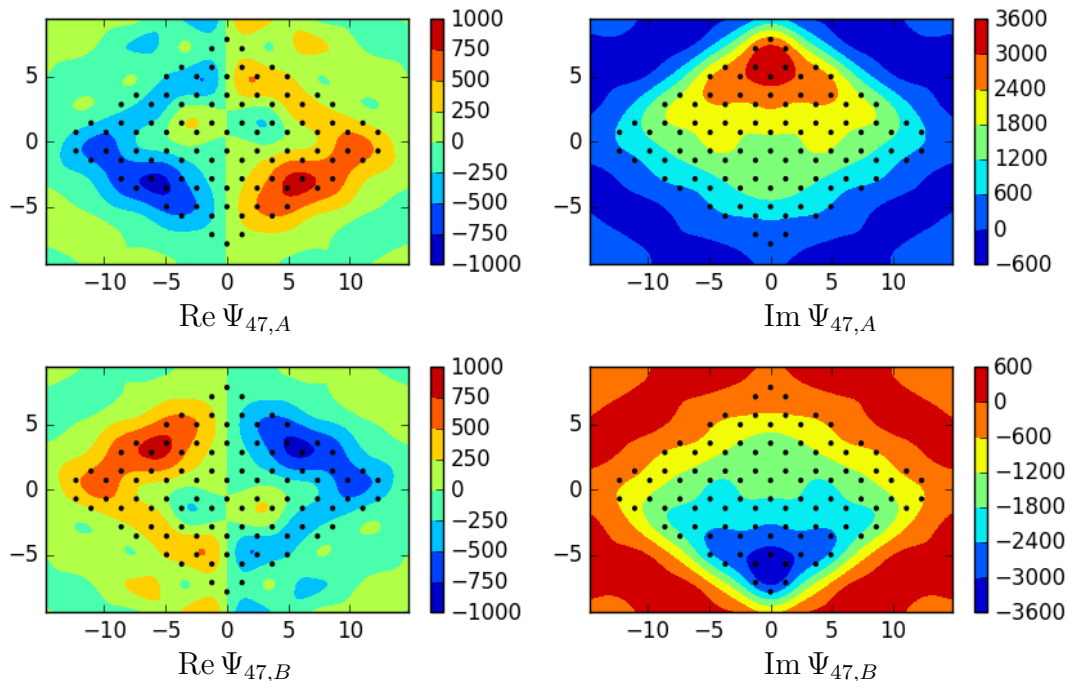


Figure B3. Real and imaginary parts of the envelope functions $\Psi_A(\mathbf{r})$ and $\Psi_B(\mathbf{r})$ for HOMO, in arbitrary units.

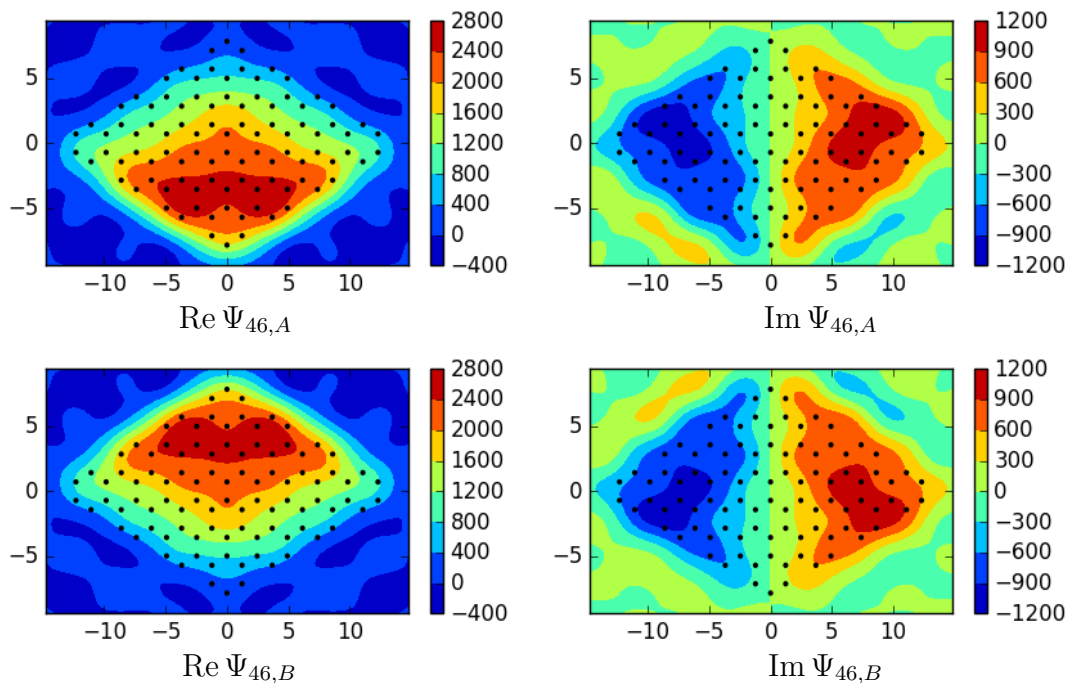


Figure B4. Real and imaginary parts of the envelope functions $\Psi_A(\mathbf{r})$ and $\Psi_B(\mathbf{r})$ for HOMO-1, in arbitrary units.

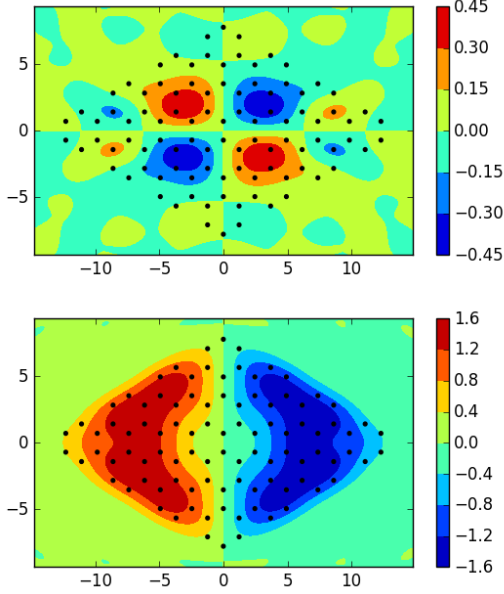


Figure B5. The smooth component of the co-densities $\psi_{46}\psi_{47}$ and $\psi_{46}\psi_{48}$ from Fig. B2: $2 \operatorname{Re}(\Psi_{46,A}^* \Psi_{47,A} + \Psi_{46,B}^* \Psi_{47,B})$ (left) and $2 \operatorname{Re}(\Psi_{46,A}^* \Psi_{48,A} + \Psi_{46,B}^* \Psi_{48,B})$ (right). Note the difference in scale maxima between the two plots.

$\Psi_{49,B} = -\Psi_{46,B}$. Let us denote $\Psi_{48,A} = \Psi_{47,A} = \tilde{\Psi}_A$, $\Psi_{48,B} = -\Psi_{47,B} = \tilde{\Psi}_B$, $\Psi_{49,A} = \Psi_{46,A} = \tilde{\Psi}_A$, $\Psi_{49,B} = -\Psi_{46,B} = \tilde{\Psi}_B$.

Let us focus on the smooth component of each co-density from Fig. B2, which can be expressed in terms of the envelope functions. For $\psi_{46}\psi_{47}$ and $\psi_{46}\psi_{48}$ they are given by $2 \operatorname{Re}(\Psi_A^* \tilde{\Psi}_A) \pm 2 \operatorname{Re}(\Psi_B^* \tilde{\Psi}_B)$, and shown in Fig. B5. For $\psi_{46}\psi_{47}$ the smooth component is much weaker, leading to the smallness of the corresponding direct Coulomb integral V_{23}^d . The reason for this is the reflection symmetry \mathcal{R}_{AB} . Indeed, with respect to this reflection, LUMO and LUMO + 1 have opposite parity (similarly to HOMO and HOMO-1). Then, $\Psi_B^*(\mathbf{r})\tilde{\Psi}_B(\mathbf{r}) = -\Psi_A^*(\mathcal{R}_{AB}\mathbf{r})\tilde{\Psi}_A(\mathcal{R}_{AB}\mathbf{r})$, so the smooth part of the co-density $\psi_{46}\psi_{47}$ is $\operatorname{Re} \Psi_A^*(\mathbf{r})\tilde{\Psi}_A(\mathbf{r}) - \operatorname{Re} \Psi_A^*(\mathcal{R}_{AB}\mathbf{r})\tilde{\Psi}_A(\mathcal{R}_{AB}\mathbf{r})$. Since $\Psi_{A,B}$ and $\tilde{\Psi}_{A,B}$ correspond to the lowest-energy orbitals, they have no oscillations (see Figs. B3 and B4, where Ψ_{47} is dominated by the imaginary part and Ψ_{46} by the real part, which have no zeros inside the GQD), so taking the difference between a point \mathbf{r} and its mirror image $\mathcal{R}_{AB}\mathbf{r}$ leads to a strong cancellation. This cancellation also persists when the mirror symmetry is not exact. As a result, the $\phi_H\phi_{H-1} = \phi_L\phi_{L+1}$ co-densities are dominated by the fast oscillating $e^{\pm 2i\mathbf{K}\mathbf{r}}$ components which leads to the smallness of corresponding direct Coulomb integral V_{23}^d .